PAPER

Check for updates

Oxide-derived low-coordination Ag catalysts enable efficient photovoltaic-driven electrochemical CO₂ reduction in MEA electrolyzers

Yanxin Xie,†[ab] Zeyu Guo, [iD]†[c] Zhikai Lang,†[a] Kezhong Liu,[ab] Jiabao Lv,[ad] Jianhua Yan,[a] Songqiang Zhu,[d] Yongzhi Zhou,[b] Bo Xu,*[e] Hao Bin Wu, [iD]*[f] Mengxia Xu*[c] and Angjian Wu [iD]*[abd]

Oxide-derived silver (Ag) catalysts have emerged as promising candidates for achieving highly efficient electrochemical CO_2 reduction reaction (eCO_2RR) to CO at industrial current densities. However, the evolution of active site configurations, the atomic-level coordination–activity relationship, and the design of practical solar-driven systems remain insufficiently explored. In this work, we report the facile *in situ* electrochemical synthesis of Ag_2O-derived Ag (Ag_2O-D-Ag), where the presence of unsaturated (low-coordination) Ag sites is revealed through operando X-ray absorption spectroscopy. The Ag_2O-D-Ag catalyst exhibits a CO faradaic efficiency of 90% at 500 mA cm^{-2} and maintains a stability over 100 hours at 200 mA cm^{-2} in a 4-cm^2 membrane electrode assembly (MEA) electrolyzer. *In situ* Fourier-transform infrared spectroscopy, combined with theoretical calculations, shows that these optimally low-coordinated Ag sites reduce the formation energy barrier of the *COOH intermediate, thereby accelerating CO production. Integration of this catalyst with a photovoltaic module enables a 100-cm^2 MEA prototype to operate stably for more than 30 hours, achieving a solar-to-CO energy efficiency of 4.87%. This study provides mechanistic insight into active site dynamics and demonstrates a scalable, renewable-energy-driven eCO_2RR system.

Broader context

The electrochemical CO_2 reduction reaction (eCO_2RR) powered by solar energy offers a promising route for mitigating the greenhouse effect. For integrated solar-driven eCO_2RR applications, it is not only essential to synthesize efficient catalysts, but also crucial to ensure stable operation of the reaction under different light conditions. Oxide-derived Ag (OD-Ag) catalysts, known for their simple synthesis process and low-coordination structure that reduces reaction energy barriers, are widely used, while the unclear coordination–activity relationship hinders their industrial applications. Moreover, while solar-driven eCO_2RR-to-CO has been widely reported, current photovoltaic systems still struggle to deliver the industrial-level current densities required for continuous operation. Herein, we clarify the coordination–activity relationship of OD-Ag catalysts through *in situ* techniques and theoretical calculations, and design efficient catalysts *via in situ* electrochemical reconstruction. By coupling a scale-up MEA electrolyzer with photovoltaic modules, we create a robust photovoltaic-electrolysis system for efficient solar-driven CO production, aimed at bridging the gap between laboratory-scale innovation and industrial feasibility.

[a] *State Key Laboratory of Clean Energy Utilization, Department of Energy Engineering, Zhejiang University, Hangzhou, 310027, Zhejiang, China. E-mail: wuaj@zju.edu.cn*

[b] *Polytechnich Institute, Zhejiang University, Hangzhou, 310058, Zhejiang, China*

[c] *Department of Chemical and Environment Engineering, University of Nottingham Ningbo China, Ningbo, 315100, China*

[d] *Baima Lake Laboratory, Hangzhou, 310053, Zhejiang, China*

[e] *Department of Battery R&D, Guangzhou Automobile Group Co., Ltd, Guangzhou, 511434, Guangdong, China*

[f] *State Key Laboratory of Silicon Materials, School of Materials Science and Engineering, Zhejiang University, Hangzhou, 310053, Zhejiang, China*

† These authors contributed equally to this work.

Introduction

The extensive use of fossil fuels has resulted in excessive carbon dioxide (CO_2) emissions, aggravating the global greenhouse effect and posing a significant barrier to sustainable societal development.[1] The electrochemical CO_2 reduction reaction (eCO_2RR), driven by renewable energy, offers a promising strategy to mitigate CO_2 emissions while producing value-added fuels and chemicals.[2–4] Among various mono-carbon[5] and multi-carbon[6,7] eCO_2RR products, carbon monoxide (CO)

stands out due to its facile separation from both liquid products and electrolytes. Moreover, CO exhibits strong market compatibility and substantial potential for downstream valorization, such as Fischer–Tropsch synthesis to produce gasoline and other multi-carbon commodities.[8] Nevertheless, realizing highly active and durable catalysts remains a critical challenge for enabling large-scale eCO$_2$RR-to-CO conversion at industrial current densities (≥ 200 mA cm^{-2}).[9,10]

Silver (Ag) is widely recognized for its effectiveness as a model catalyst for eCO$_2$RR-to-CO, attributable to its enhanced *CO desorption and suppressed hydrogen evolution reaction (HER), and is considered as a robust commercial catalyst for future large-scale eCO$_2$RR.[11] Among Ag-based catalysts, oxide-derived Ag (OD-Ag) has attracted particular attention due to its tunable coordination structure.[1,12] The conversion of Ag oxides into OD-Ag involves the elimination of oxygen atoms and the formation of low-coordination Ag sites.[13] Theoretical studies demonstrate that these low-coordinated Ag sites lower the energy barrier for CO$_2$ reduction and enhance electrocatalytic activity by stabilizing reaction intermediates.[13,14] Despite these advances, the potential-driven evolution of the coordination structure and the coordination–activity relationship remain insufficiently understood. Therefore, real-time probing of the catalyst's coordination environment during an electroreduction process is crucial to achieve selective and stable eCO$_2$RR-to-CO.

Beyond electrocatalyst design, implementing the eCO$_2$RR at scale demands not only large electrolyzers but also effective integration with photovoltaic (PV) systems for direct solar utilization. Sacco et al. first reported an integrated solar-driven electrochemical device for CO$_2$-to-CO conversion, achieving a CO faradaic efficiency (FE) of 78% over 3 hours.[15] Subsequent advances included gas-fed flow cell devices capable of operating at higher current densities, such as 98.3 mA cm^{-2} under simulated sunlight.[16] However, most existing PV systems remain unable to provide the stable, industrial-level current densities necessary for sustained eCO$_2$RR-to-CO operation. The membrane electrode assembly (MEA) configuration, featuring a zero-gap design and gas diffusion electrodes, enables high product selectivity, current density, and energy efficiency through efficient mass transport.[17] Additionally, assembling multiple MEAs into a cell stack facilitates industrial-scale operation.[18] Therefore, integrating MEA-based electrolyzers with PV modules capable of stable power delivery is essential to bridge the gap between the bench- and large-scale eCO$_2$RR.

In this work, we report the synthesis of Ag$_2$O-derived Ag (Ag$_2$O-D-Ag) with an unsaturated coordination structure via in situ electrochemical reconstruction within an MEA electrolyzer. This catalyst achieved a FE$_{CO}$ of 90% at 500 mA cm^{-2} and exhibited remarkable operation stability for over 100 hours at 200 mA cm^{-2}. Operando X-ray absorption spectroscopy (XAS) was employed to elucidate the dynamic evolution of the Ag coordination structure and to confirm the optimal coordination number for eCO$_2$RR-to-CO. Complementary in-situ Fourier-transform infrared (FTIR) spectroscopy and density functional theory (DFT) calculations confirmed that Ag$_2$O-D-Ag can lower the formation energy of *COOH, thereby facilitating the CO

formation. A 100-cm^2 MEA electrolyzer was coupled with a photovoltaic module and operated stably at 4.5 V for 30 hours, delivering an average current exceeding 20 A while maintaining a FE$_{CO}$ above 91%. This system achieved a solar-to-CO energy efficiency of 4.87% and an affordable levelized cost of CO, indicating its significant economic feasibility and potential for industrial applications. By integrating scaled MEAs with photovoltaic modules, this study provides new horizons for bridging the gap between laboratory-scale innovation and industrial feasibility.

Results and discussion

Synthesis and characterization

Ag$_2$O-derived Ag (Ag$_2$O-D-Ag) catalysts, featuring unsaturated coordinated Ag sites, were synthesized via in situ electroreduction of as-prepared Ag$_2$O pre-catalysts within an MEA electrolyzer (Fig. 1a and Fig. S1, S2, SI). Scanning electron microscopy (SEM) analysis revealed that the as-synthesized Ag$_2$O pre-catalysts underwent significant reconstruction during electroreduction, resulting in a distinctive cracked nanoparticle (NP)-like morphology (Fig. 1b and Fig. S3, S4, SI). Surface elemental analysis through energy-dispersive X-ray spectroscopy (EDS) demonstrated a significant reduction in the oxygen content in the Ag$_2$O-D-Ag compared to the pristine pre-catalysts (Fig. S5, SI). Transmission electron microscopy (TEM) provided further insights into the structural and phase evolution of Ag$_2$O-D-Ag (Fig. S6, SI), confirming the emergence of smaller nanoparticles with cracked surfaces post-electroreduction. To investigate how the presence of smaller nanoparticles affects catalytic performance, two catalyst models with different particle sizes were constructed and analyzed through simulations using COMSOL 6.3 (Fig. S7 and Table S1, SI). The simulations reveal that the catalyst with smaller particle sizes possesses a larger specific surface area and more active reaction sites, thereby enhancing its catalytic performance (Fig. S8–S11, SI). High-resolution TEM images identified the presence of the Ag (111) crystal facet as the dominant feature in Ag$_2$O-D-Ag, further confirming the reduction of Ag$_2$O. Ex situ X-ray diffraction (XRD) patterns of Ag$_2$O-D-Ag before and after 10-min electrochemical reconstruction at -0.8 V vs. RHE indicated a gradual transition from Ag$_2$O to metallic Ag (Fig. 1c and Fig. S12, SI). Complementary, time-resolved ex situ X-ray photoelectron spectroscopy (XPS) of Ag 3d (Fig. 1c and Fig. S13, SI) showed a progressive shift of the Ag$^+$ peak associated with Ag$_2$O to the Ag^0 peak at -0.8 V vs. RHE during a 10-min eCO$_2$RR process, confirming the emergence of metallic Ag as the predominant phase in Ag$_2$O-D-Ag.[19] These collective results confirmed that Ag$_2$O pre-catalysts were reduced to Ag$_2$O-D-Ag with a metallic Ag phase.

Operando X-ray absorption spectroscopy (XAS) was conducted at -0.8 V vs. RHE to provide atomic-level insights into the dynamic evolution and origins of electrocatalytic activity in Ag$_2$O-D-Ag during electrolysis.[20,21] To assess the role of unsaturated coordinated Ag sites in the eCO$_2$RR, control samples of metallic Ag and AgO-derived Ag (AgO-D-Ag) were also
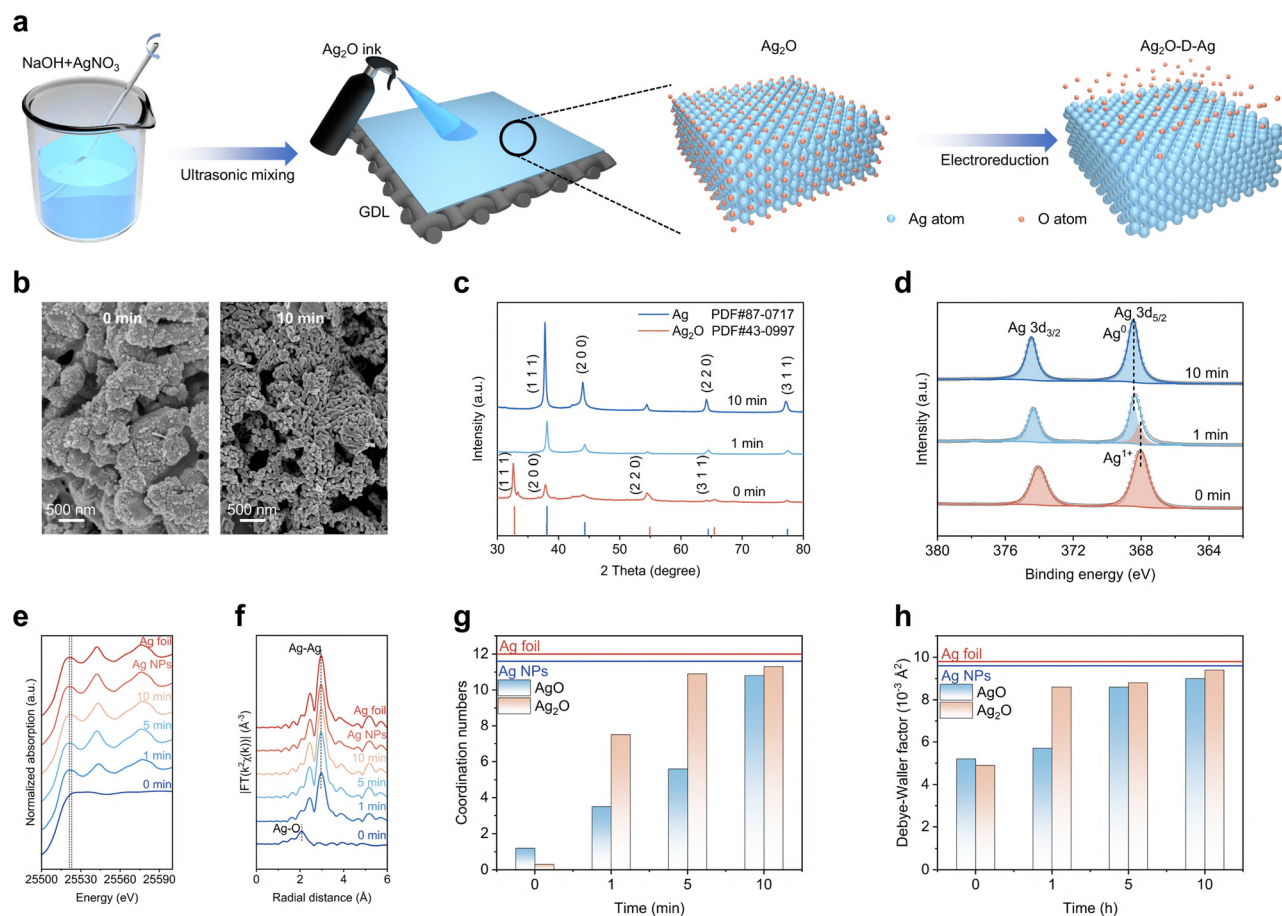
Fig. 1 Dynamic configuration evolution of Ag oxides to their derived Ag. (a) Schematic illustration of Ag$_2$O-D-Ag synthesis. (b) Time-dependent SEM images of Ag$_2$O. (c) Time-dependent *ex situ* XRD patterns of Ag$_2$O. (d) Time-dependent *ex situ* Ag 3d XPS spectra of Ag$_2$O. (e) Time-dependent normalized Ag K-edge XANES spectra of Ag$_2$O. (f) Time-dependent Fourier transform of the Ag K-edge EXAFS spectra (R-space) of Ag$_2$O. (g) Time-dependent Ag–Ag bond coordination number (CN) of Ag foil, Ag NPs, AgO, and Ag$_2$O. (h) Time-dependent DW of the Ag–Ag bond for Ag foil, Ag NPs, AgO, and Ag$_2$O. All measurements were performed at −0.8 V *vs.* RHE (without iR compensation) in 0.01 M KHCO$_3$ for 10 minutes.

synthesized from different precursors using the MEA electrolyzer for direct comparison. *In situ* electrochemical reconstruction experiments were carried out in a dedicated reactor containing 0.01 M KHCO$_3$ saturated with CO$_2$ (Fig. S14 and S15, SI). During a 10-minute dynamic reconstruction process, XAS revealed a gradual transition of the characteristic Ag$^+$ peak (from Ag$_2$O) and Ag^{2+} (from AgO) to the Ag^0 peak, indicating reduction of both oxides to metallic Ag. Notably, Ag$_2$O transitioned to Ag^0 more rapidly than AgO (Fig. 1d, e and Fig. S16a, S17a).[22] These transformations were further corroborated by extended X-ray absorption fine structure (EXAFS) analysis using a Fourier-transformed K^2-weighted $\chi(k)$ function, characteristic Ag–O scattering signals of AgO (at 2.05 Å) and Ag$_2$O (at 2.08 Å) gradually disappeared, while the metallic Ag–Ag bonding signal (at 2.86 Å) increased over time (Fig. 1f and Fig. S16b, S17b, SI).[13]

To elucidate changes in the local structure during reconstruction, EXAFS spectra of AgO and Ag$_2$O were fitted (Fig. S18, SI).[23] The reliability of these fits was confirmed by comprehensive fitting parameters (Table S2, SI), alongside plots in k-space (Fig. S19, SI) and R-space (Fig. S20, SI). As shown in Fig. 1f and Fig. S21 (SI), the Ag–Ag coordination number in both Ag$_2$O and

AgO increased steadily throughout the *in situ* dynamic reconstruction. Specifically, the coordination number of Ag–Ag bonds in Ag$_2$O-D-Ag ($\sim$11.3) was found to be lower than those of Ag NPs ($\sim$11.6) and Ag foil ($\sim$12.0), but higher than that in AgO-D-Ag ($\sim$10.8) (Fig. 1g). Additionally, the Debye–Waller (DW) factor σ^2, derived from EXAFS fitting and related to Ag–Ag bond fluctuations, exhibited an inverse correlation with the coordination number (Fig. 1h).[24] The DW factor for the Ag–Ag bond in Ag$_2$O-D-Ag ($\sim$9.4 $\times$ 10^{-3} Å^2) was lower than that in AgO-D-Ag ($\sim$9.0 $\times$ 10^{-3} Å^2), but higher than those observed for Ag NPs ($\sim$9.6 $\times$ 10^{-3} Å^2) and Ag foil ($\sim$9.8 $\times$ 10^{-3} Å^2). Collectively, these results demonstrate that both Ag$_2$O and AgO reach dynamic equilibrium during *in situ* reconstruction, resulting in catalysts with distinct low-coordination states.

Electrochemical CO$_2$ reduction performance

Following *in situ* electrochemical reconstruction, Ag$_2$O-D-Ag exhibited the most favorable electrochemical properties among the tested catalysts in the MEA electrolyzer. Linear sweep voltammetry (LSV) revealed that Ag$_2$O-D-Ag displayed the lowest onset cell voltage of 2.34 V, outperforming both AgO-D-Ag
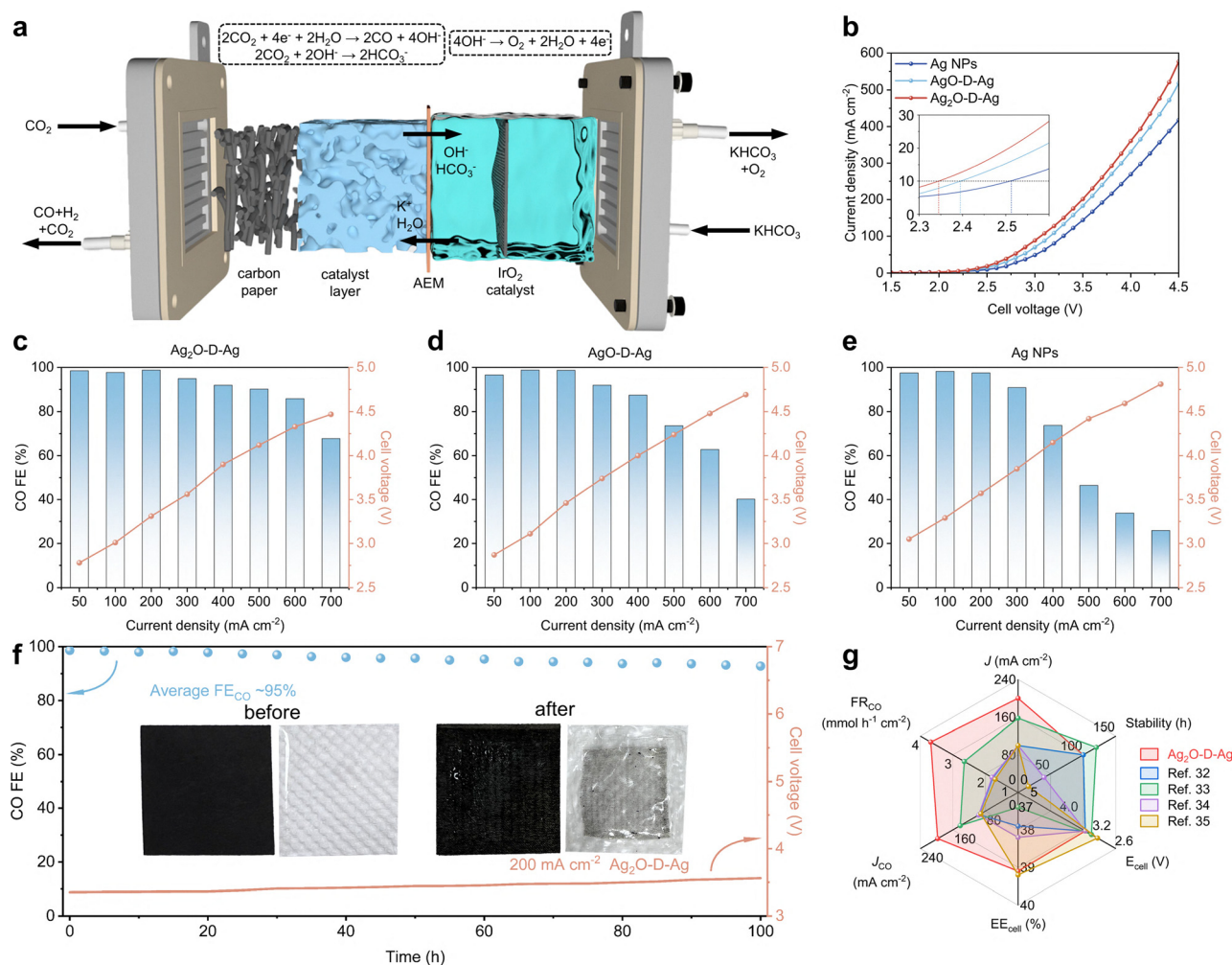
Fig. 2 eCO$_2$RR performance of Ag$_2$O-D-Ag. (a) Schematic illustration of the MEA electrolyzer measurement setup. (b) LSV curves from 1.5 to 4.5 V for Ag$_2$O-D-Ag, AgO-D-Ag, and Ag NPs in a 4-cm^2 MEA electrolyzer. FECO and cell voltage of (c) Ag$_2$O-D-Ag, (d) AgO-D-Ag, and (e) Ag NPs recorded across a current density range from 50 to 700 mA cm^{-2} in the 4-cm^2 MEA electrolyzer. (f) Stability measurement (red line) and corresponding FECO (blue dots) of Ag$_2$O-D-Ag in the 4-cm^2 MEA electrolyzer at a constant total current density of 200 mA cm^{-2}. Inset photographs show the Ag$_2$O-D-Ag catalyst and anion exchange membrane (AEM) surface before and after 100 hours of operation. (g) Comparative performance summary of cell voltage (E_{cell}), stability, CO formation rate, total current density, partial CO current density (J_{CO}), and cell energy efficiency with recently reported state-of-the-art eCO$_2$RR-to-CO catalysts in the MEA electrolyzer.

(2.39 V) and Ag NPs (2.51 V) (Fig. 2a and b and Fig. S22, SI). Moreover, at an applied potential of 4.5 V, Ag$_2$O-D-Ag achieved a current density of 576.5 mA cm^{-2}, surpassing those of AgO-D-Ag (517.2 mA cm^{-2}) and Ag NPs (417.7 mA cm^{-2}). The turnover frequency (TOF) of Ag$_2$O-D-Ag was calculated to be 1250 h^{-1} at 4.5 V, outperforming those of AgO-D-Ag (1040 h^{-1}) and Ag NPs (841 h^{-1}) (Fig. S23, SI). Under identical loading conditions, the remarkably high TOF of Ag$_2$O-D-Ag could be attributed to its intrinsic catalytic activity. The electrochemical surface area (ECSA) was assessed *via* cyclic voltammetry (CV) at varying scan rates in a standard three-electrode setup, with the electrochemical double-layer capacitance (C_{dl}) being used as an indicator (Fig. S24, SI). Ag$_2$O–D-Ag exhibited the highest C_{dl} value (2.0 mF cm^{-2}) compared to AgO-D-Ag (1.75 mF cm^{-2}) and Ag NPs (0.67 mF cm^{-2}), reflecting a greater electrochemical active surface area and enhanced eCO$_2$RR activity. Kinetic analysis using Tafel slope measurements further

confirmed the superior catalytic behavior of Ag$_2$O-D-Ag, which presented a Tafel slope of 154.51 mV dec^{-1}, substantially lower than that of AgO-D-Ag (217.73 mV dec^{-1}) and Ag NPs (410.53 mV dec^{-1}) (Fig. S25 and S26, SI). Additionally, electrochemical impedance spectroscopy (EIS) revealed that Ag$_2$O-D-Ag had the lowest charge-transfer resistance (R_{ct}) at 10.9 Ω, compared to 27.8 Ω for AgO-D-Ag and 37.5 Ω for Ag NPs, indicating faster interfacial electron transfer dynamics (Fig. S27, SI).

The FE$_{CO}$ values of Ag$_2$O-D-Ag, AgO-D-Ag and Ag were systematically evaluated across a current density range of 50 to 700 mA cm^{-2} in a 4-cm^2 MEA electrolyzer (Fig. 2c–e and Fig. S28, S29, SI). Notably, at an industrially relevant current density of 500 mA cm^{-2}, Ag$_2$O-D-Ag exhibited a FE$_{CO}$ of 90.1%, substantially higher than that of AgO-D-Ag (73.6%) and Ag NPs (46.5%), highlighting its superior CO selectivity under high current operation. Moreover, at 700 mA cm^{-2}, all three catalysts

exhibit a noticeable decline in FE_{CO} to varying degrees, primarily due to salt precipitation (Fig. S30, SI). High current densities intensify the electro-osmotic effect, driving more hydrated K^+ cations from the anode to the cathode side, where they combine with HCO_3^- to form $KHCO_3$ precipitates in the cathode flow channel.[25,26] Reducing the concentration of alkali metal cations in the anolyte,[27] completely eliminating alkali metal cations,[28] or operating a bipolar membrane (BPM) under reverse bias has been proven effective in suppressing K^+ migration.[29] To further evaluate catalyst durability, eCO_2RR-to-CO stability tests were conducted at 200 mA cm^{-2}. As shown in Fig. 2f and Fig. S31 (SI), Ag$_2$O-D-Ag delivered remarkable stability and maintained high selectivity for 100 hours in the MEA electrolyzer, outperforming AgO-D-Ag (75 hours) and Ag NPs (65 hours). Post-stability testing, a small amount of Ag$_2$O-D-Ag was observed adhering to the AEM, likely due to pressure differences at the triple-phase interface during the eCO_2RR.[30] Due to the low $KHCO_3$ concentration and the high CO_2 utilization efficiency enabled by the optimal coordination state of Ag$_2$O-D-Ag, only minimal salt precipitation was observed in the flow channels after prolonged operation.[31] Building on this,

extended-duration testing revealed a markedly accelerated decline in FE_{CO}, accompanied by evident salt precipitation in the cathode flow channel (Fig. S32, SI). After rinsing the channel with deionized water and resuming the measurement, FE_{CO} recovered to $\sim$90%, indicating that salt precipitation was the primary cause of performance degradation during the stability measurement. Importantly, at a cell voltage of 3.4 V, Ag$_2$O-D-Ag achieved an average FE_{CO} of approximately 95% with a cell energy efficiency (EE) of 39.1% and a CO formation rate of 3.68 mmol h^{-1} cm^{-2}, all of which surpass the performance of AgO-D-Ag and Ag NPs (Table S3, SI). The unique, optimally coordinated Ag sites in Ag$_2$O-D-Ag offer superior electrocatalytic activity and long-term durability, outperforming previously reported state-of-the-art eCO_2RR-to-CO catalysts in MEA electrolyzers (Fig. 2g), thus identifying Ag$_2$O-D-Ag as a promising candidate for industrial-scale eCO_2RR-to-CO conversion.[32–35]

Mechanistic analysis

To elucidate the mechanism of eCO_2RR-to-CO on oxide-derived Ag-based catalysts, *in situ* Fourier transform infrared (FTIR)
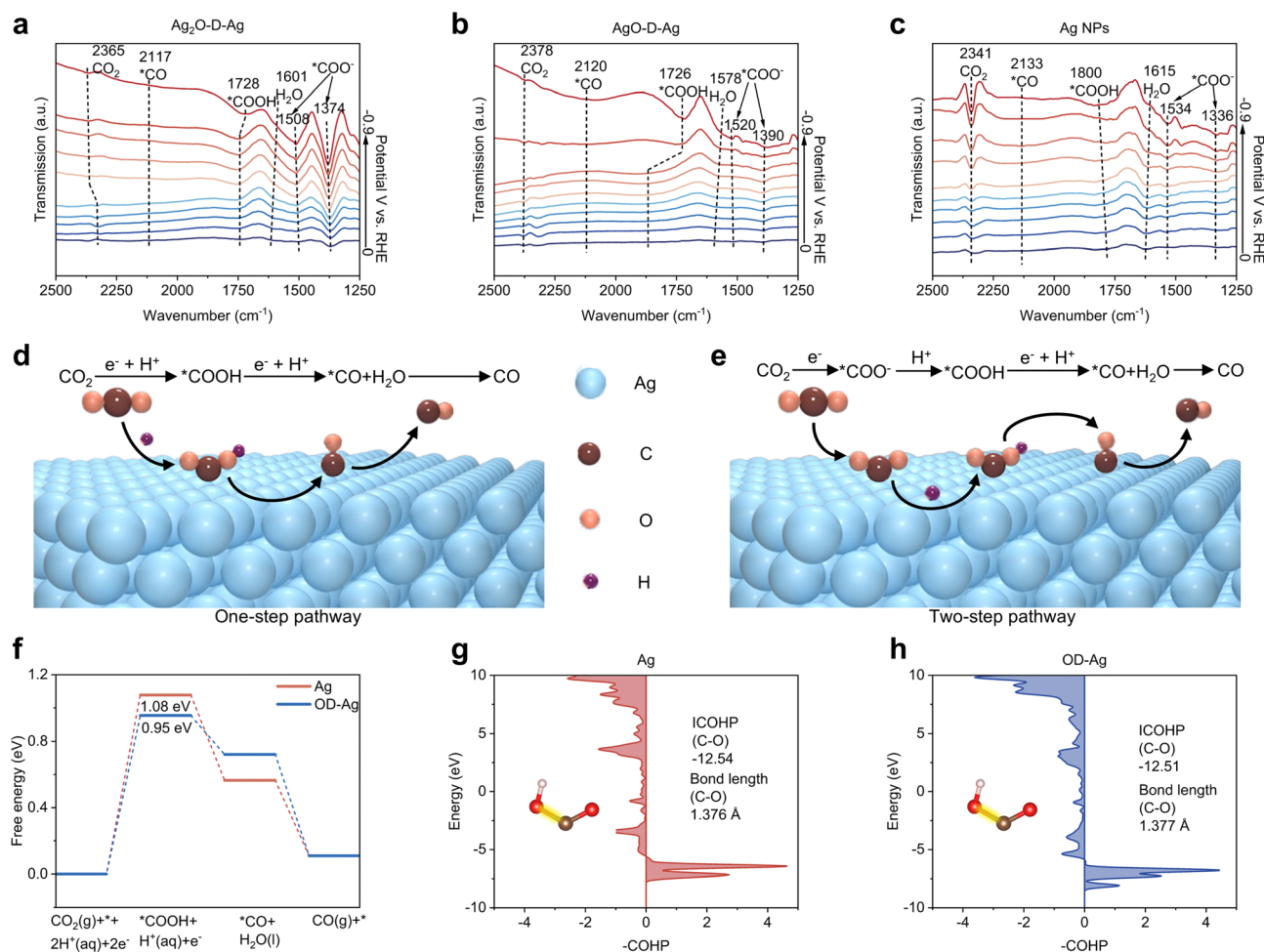
Fig. 3 Catalytic mechanism of Ag$_2$O-D-Ag. *In situ* FTIR spectra of (a) Ag$_2$O-D-Ag, (b) AgO-D-Ag, and (c) Ag NPs in a custom reactor containing 0.01 M KHCO$_3$ saturated with CO$_2$ across −0.9 to 0 V *vs.* RHE (without *iR* compensation). Schematic illustration of two reaction pathways on Ag-based catalyst surfaces: (d) a one-step and (e) a two-step sequential mechanism. (f) Calculated free energy diagrams of the eCO_2RR-to-CO process on Ag and OD-Ag. COHP analysis of the C–O interaction on (g) Ag (111) and (h) OD-Ag (111).

spectroscopy was employed to monitor the evolution of reaction intermediates on Ag_2O-D-Ag, AgO-D-Ag, and Ag NPs in CO_2-saturated 0.01 M $KHCO_3$ over a potential range from 0 to −0.9 V vs. RHE (Fig. S33, SI). As shown in Fig. 3a, Ag_2O-D-Ag exhibited pronounced absorption bands at 1374 cm^{-1} and 1508 cm^{-1}, attributed to monodentate carbonate (*COO^-) species. The intensities of these bands were significantly higher than those observed for AgO-D-Ag (1390 cm^{-1} and 1520 cm^{-1}) and Ag NPs (1336 cm^{-1} and 1534 cm^{-1}) in Fig. 3b and c.[36] Moreover, Ag_2O-D-Ag exhibited a distinct absorption band at 1728 cm^{-1}, corresponding to the *COOH intermediate, with an intensity comparable to AgO-D-Ag (1726 cm^{-1}, Fig. 3b) and significantly stronger than Ag NPs (1800 cm^{-1}, Fig. 3c).[35] Kortlever et al. demonstrated that *COOH formation proceeds via two distinct mechanisms: a concerted proton-coupled electron transfer (PCET) step (Fig. 3d), or a sequential transfer mechanism in which electrons and protons are transferred in separate steps (Fig. 3e).[37] These results indicated that, for both Ag_2O-D-Ag and AgO-D-Ag, a substantial portion of absorbed CO_2 is sequentially converted to *COO^- and subsequently *COOH, with *COOH acting as the key intermediate for proton transfer during eCO_2RR-to-CO. Relative to AgO-D-Ag and Ag, Ag_2O-D-Ag more efficiently activate CO_2 to form *COO^- and promotes the subsequent protonation to *COOH, thereby accelerating the rate-determining step (RDS) of eCO_2RR-to-CO.

To gain deeper insight into the enhanced electrocatalytic activity of OD-Ag, density functional theory (DFT) calculations were carried out to compare the reaction energetics and electronic structures of OD-Ag and metallic Ag. Previous studies have established that OD-Ag undergoes lattice relaxation following in situ electrochemical reconstruction due to oxygen removal, resulting in structural collapse and the development of unsaturated coordination sites.[13,38] An Ag slab model with a collapsed surface structure was constructed to simulate OD-Ag (111) (Fig. S34, SI).[39] This involved selectively removing Ag atoms from the Ag (111) surface to generate the OD-Ag (111) model. Post-optimization, the lattice parameters of OD-Ag (111) remained consistent with pristine Ag (111) (Table S4, SI). While earlier reports attributed the superior electrocatalytic activity of OD-Ag to reconstructed surface physicochemical properties, the detailed mechanistic pathway during the eCO_2RR has remained elusive.[14] Building upon in situ FTIR identification of *COOH and *CO intermediates, DFT calculations evaluated changes in adsorption properties and thermodynamic profiles for the eCO_2RR pathway. As shown in Fig. 3f, the formation of *COOH exhibited the highest reaction free energy on both the Ag (111) and OD-Ag (111) slab models, indicating that the conversion of CO_2 to *COOH via protonation constitutes the RDS. Notably, the reaction free energy for *COOH adsorption on OD-Ag (111) was 0.95 eV, lower than that observed for Ag (111) (1.08 eV). Thus, the presence of low-coordination structures in OD-Ag effectively lowers the energy barrier for *COOH formation, enhancing the selectivity and activity of the eCO_2RR-to-CO process.

To gain deeper insight into the origin of the free energy optimization observed during *COOH formation on the OD-Ag surface, a systematic examination of adsorption configurations was performed. On the Ag (111) surface, the most stable configuration of the *COOH intermediate is at the top site, with the carbon atom positioned directly above a silver atom (C–Ag distance: 2.16 Å), and the O–C–O plane oriented nearly perpendicular to the catalyst surface (Fig. S35a and c, SI).[13] In contrast, on OD-Ag, *COOH preferentially interacts with Ag atoms in the second atomic layer within the collapsed region, which features a lower coordination state (C–Ag distance: 2.20 Å) (Fig. S35b and d, SI). This configuration results in a slight tilt in the O–C–O plane and enables the carbonyl oxygen atom to additionally interact with a silver atom (O–Ag distance: 2.49 Å). These changes indicate enhanced *COOH activation on OD-Ag (111) compared to the Ag (111) surface. To further assess these interactions, crystal orbital Hamiltonian population (COHP) analysis was conducted to analyze the bonding strength between the carbon and hydroxyl oxygen atoms in *COOH (Fig. 3g and h). The integrated COHP (ICOHP) value serves as a measure of the C–O bonding interaction, where a more negative value indicates a stronger coupling between the C and O atoms.[40] The ICOHP value for the C–O bond in *COOH on the OD-Ag (111) model (−12.51) is less negative than on the Ag (111) slab (−12.54), indicating weaker C–O coupling. Moreover, this bond is elongated to 1.377 Å on OD-Ag (111), confirming a greater readiness for bond cleavage. Thus, the *COOH intermediate on OD-Ag (111) more readily undergoes transformation to *CO. Overall, these findings demonstrate that the low-coordination structures of OD-Ag reduce the binding energy and activate the configuration of the key *COOH intermediate, effectively facilitating the pivotal conversion step of eCO_2RR-to-CO.

Solar-driven CO_2 reduction and techno-economic analysis

The feasibility of utilizing renewable energy for CO production was assessed by coupling the MEA electrolyzer with a photovoltaic module, thus forming a photovoltaic-electrolysis (PV-EC) system (Fig. 4a). Monitoring the 24-hour performance of the PV module under varying weather conditions revealed significant fluctuations in power output depending on time and weather, which can impede consistent energy supply to the eCO_2RR process (Fig. 4b–d). To meet industrial operation standards, electrocatalytic testing was performed in a 100-cm^2 MEA electrolyzer, which required a cell voltage of approximately 4.4 V to maintain a current density of 200 mA cm^{-2}, achieving the FE_{CO} to 92% (Fig. S36, SI). To achieve a reliable and continuous power supply for the eCO_2RR, a complete PV-EC system was developed, consisting of a commercial solar panel (77 cm × 67 cm), a 200 Wh battery module for energy storage, a DC/DC converter to lower and stabilize the voltage to 4.5 V, and the MEA electrolyzer itself (Fig. 4e). The maximum power point tracking (MPPT) regulates the photovoltaic panel voltage, with the battery ensuring output stability, while a DC/DC converter delivers the desired output voltage. Under simulated AM 1.5G 1-sun irradiation, the I–V curve of the photovoltaic module exhibited an open-circuit voltage of 22.4 V, a short-circuit
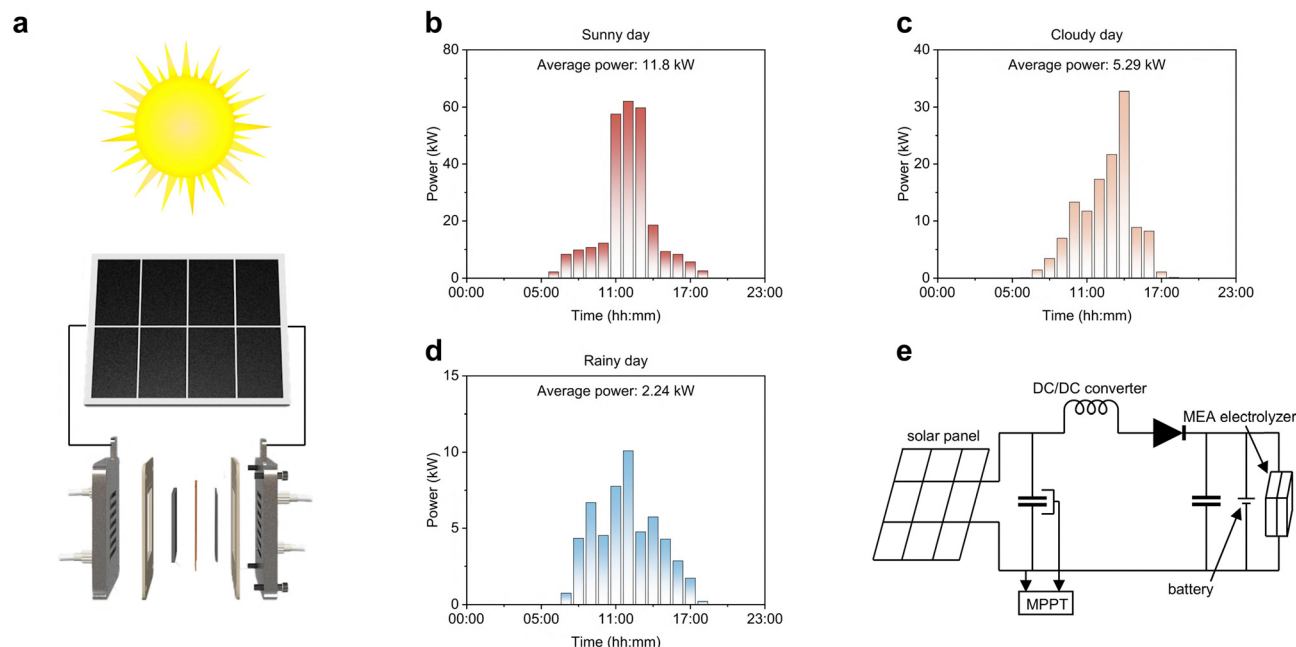
Fig. 4 Construction of the photovoltaic-electrolysis (PV-EC) system. (a) Schematic illustration of the PV-EC system. The daily output power of an actual photovoltaic module under (b) sunny day, (c) cloudy day, and (d) rainy conditions. (e) Equivalent circuit diagram of the complete PV-EC setup.

current of 6.08 A, and a maximum power point (MPP) at 17.4 V and 5.75 A (Fig. S37 and S38, SI).

As shown in Fig. 5(a), this PV module was directly coupled to the 100-cm^2 MEA electrolyzer to facilitate solar-driven, industrial-scale eCO$_2$RR to CO. Under simulated AM 1.5G 1-sun irradiation conditions, the system maintained stable operation at a cell voltage of 4.5 V for a duration of 30 hours, with an average current exceeding 20 A (Fig. 5b). Powered by the PV module, the Ag$_2$O–D-Ag catalyst achieved a full-cell energy efficiency (EE) of 27.9%, a total CO formation rate of 9.87 g h^{-1}, and a solar-to-CO (STC) EE of 4.87%. The outstanding electro-catalytic activity and stability of Ag$_2$O-D-Ag in the scaled-up
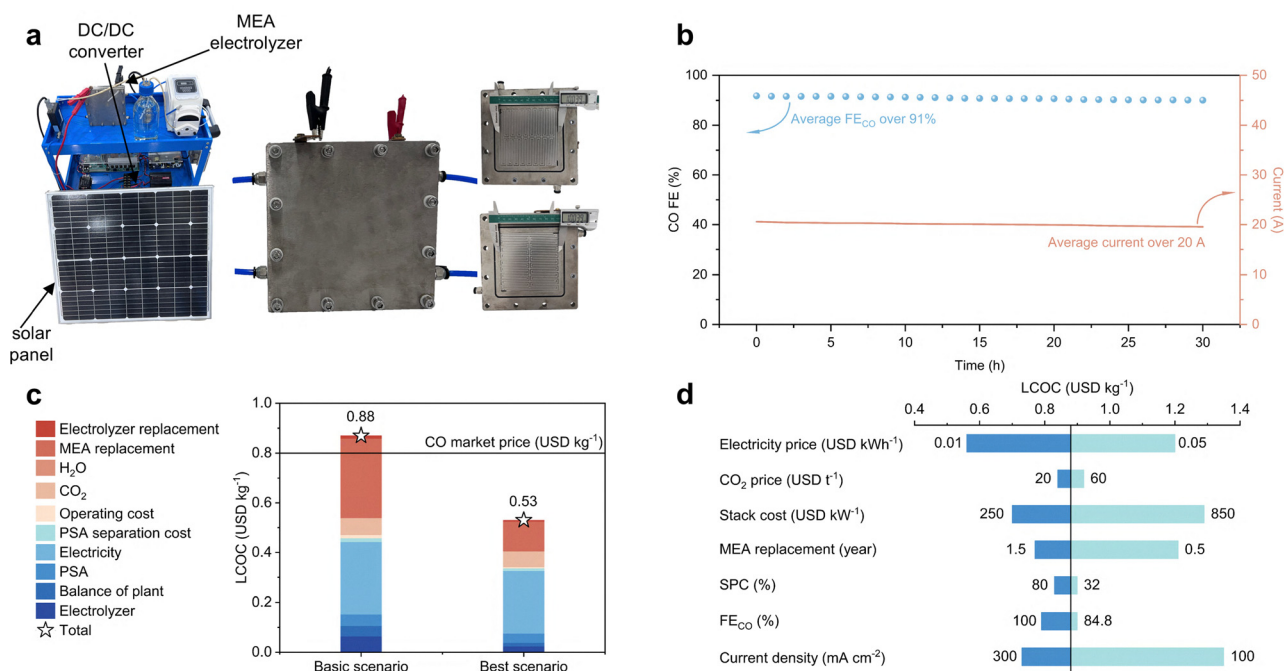

Fig. 5 Solar-driven scale-up CO$_2$ reduction. (a) Digital image of the complete PV-EC setup. (b) Stability testing (red line) and corresponding FE$_{CO}$ (blue dots) for Ag$_2$O-D-Ag in the 100-cm^2 MEA electrolyzer at a constant cell voltage of 4.5 V. (c) Techno-economic analysis (TEA) of eCO$_2$RR-to-CO comparing a basic scenario with a best scenario. (d) Single-variable sensitivity analysis for the LCOC in the basic scenario.

MEA electrolyzer are attributed to its excellent intrinsic catalytic properties. In the scaled-up MEA electrolyzer, uneven current density distribution occurs, with certain regions exhibiting current densities higher than the average.[41] In the 4-cm^2 MEA electrolyzer, Ag$_2$O-D-Ag demonstrated impressive electrocatalytic activity and stability across a broad range of current densities, making it well-suited to operate under conditions of uneven current density.

To assess the future economic viability of eCO$_2$RR technology, a techno-economic analysis (TEA) of the eCO$_2$RR-to-CO process is performed. The TEA model primarily comprises the following steps: flue gas is captured and purified into high-purity CO$_2$ via carbon capture technologies, which is then electrochemically reduced to CO using H$_2$O as the reactant in a MEA electrolyzer. The produced CO is further purified through PSA technology, while unreacted CO$_2$ is recycled back into the MEA electrolyzer for continued conversion. The economic viability of Ag$_2$O-D-Ag in the 100-cm^2 MEA system was evaluated using current performance data as the basic scenario, while a best-case scenario was projected by factoring in continued advances in the eCO$_2$RR technology. The key parameters are provided in Tables S5 and S6 (SI). As shown in Fig. 5c, under the base scenario, the levelized cost of CO (LCOC) via the eCO$_2$RR was estimated to be 0.88 USD k^{-1}. Under the best scenario, where the eCO$_2$RR operates at a current density of 500 mA cm^{-2}, achieves 100% FECO, and 80% CO$_2$ single-pass conversion (SPC), the LCOC drops to 0.53 USD kg^{-1}, falling below the current market price of CO (0.80 USD kg^{-1}), thereby demonstrating promising economic viability (Tables S7–S9, SI). To provide theoretical guidance for future eCO$_2$RR development, a sensitivity analysis was conducted on various performance parameters based on the base scenario, as illustrated in Fig. 5d and Table S10 (SI). Among all the parameters, a reduction in electricity price offers the greatest potential for lowering the LCOC. The photovoltaic module, when coupled with the MEA electrolyzer, supplies green electricity to drive the reaction, significantly reducing the LCOC and paving the way for maximizing the profitability of eCO$_2$RR technology.

Conclusions

In this work, local unsaturated coordination states of Ag active sites on Ag$_2$O-D-Ag were successfully engineered through in situ electroreduction within an MEA electrolyzer. The Ag$_2$O-D-Ag catalyst achieved a CO FE exceeding 90% across a wide current density window of 50–500 mA cm^{-2}, and demonstrated operational stability for over 100 hours at a current density of 200 mA cm^{-2} in a 4-cm^2 MEA cell. Operando XAS analyses during eCO$_2$RR-to-CO revealed that the Ag sites undergo structural reconstruction, leading to the formation of low coordination environments that enhance current density, stability and faradaic efficiency. Additionally, a combination of in situ FTIR spectroscopy and DFT calculations revealed that Ag$_2$O-D-Ag with optimized low-coordination sites effectively reduces the energy barrier for *COOH formation, thereby facilitating highly

efficient and selective conversion of CO$_2$ to CO. The Ag$_2$O-D-Ag catalyst further displayed robust electrocatalytic activity and durability in a photovoltaic-coupled 100-cm^2 MEA device. By optimizing the integrated PV-EC configuration, a solar-to-CO (STC) conversion efficiency of 4.87% was achieved, alongside a levelized CO production cost of 0.88 USD kg^{-1} and sustained eCO$_2$RR operation at an average current of 20 A for 30 hours. These findings underscore the significant potential of integrating photovoltaic cells with MEA electrolyzers to realize cost-effective and commercially viable solar-driven eCO$_2$RR systems.

Author contributions

Yanxin Xie: writing – original draft, validation, investigation, data curation, and conceptualization. Zeyu Guo: visualization, validation, methodology, and formal analysis. Zhikai Lang: software, methodology, and formal analysis. Kezhong Liu: visualization, resources, and formal analysis. Jiabao Lv: software, resources, and formal analysis. Jianhua Yan: resources and formal analysis. Songqiang Zhu: resources and formal analysis. Yongzhi Zhou: visualization, resources, and methodology. Bo Xu: Software, Formal analysis. Hao Bin Wu: writing – review and editing, validation, and supervision. Mengxia Xu: writing – review and editing, validation, supervision, funding acquisition, and conceptualization. Angjian Wu: writing – review and editing, writing – original draft, validation, project administration, and funding acquisition.

Conflicts of interest

The authors declare that they have no known competing financial interests or personal relationships that could have appeared to influence the work reported in this paper.

Data availability

The data supporting the findings of this study are available within the article and its SI. See DOI: **https://doi.org/10.1039/d5ey00208g**.

Acknowledgements

References

1 Y. Y. Birdja, E. Pérez-Gallent, M. C. Figueiredo, A. J. Göttle, F. Calle-Vallejo and M. T. M. Koper, *Nat. Energy*, 2019, **4**, 732–745.

2 B. Rosen, A. Salehi-Khojin, M. Thorson, W. Zhu, D. Whipple, P. Kensi and R. Masel, *Science*, 2011, **334**, 643–644.

3 M. Liu, Y. Pang, B. Zhang, P. De Luna, O. Voznyy, J. Xu, X. Zheng, C. T. Dinh, F. Fan, C. Cao, F. P. G. de Arquer, T. S. Safaei, A. Mepham, A. Klinkova, E. Kumacheva, T. Filleter, D. Sinton, S. O. Kelley and E. H. Sargent, *Nature*, 2016, **537**, 382–386.

4 S. Lin, C. S. Diercks, Y. Zhang, N. Kornienko, E. M. Nichols, Y. Zhao, A. R. Paris, D. Kim, P. Yang, O. M. Yaghi and C. J. Chang, *Science*, 2015, **349**, 1208–1213.

5 R. G. Mariano, K. McKelvey, H. S. White and M. W. Kanan, *Science*, 2017, **358**, 1187–1192.

6 C.-T. Dinh, T. Burdyny, M. G. Kibria, A. Seifitokaldani, C. M. Gabardo, F. P. García de Arquer, A. Kiani, J. P. Edwards, P. De Luna, O. S. Bushuyev, C. Zou, R. Quintero-Bermudez, Y. Pang, D. Sinton and E. H. Sargent, *Science*, 2018, **360**, 783–787.

7 K. Jiang, R. B. Sandberg, A. J. Akey, X. Liu, D. C. Bell, J. K. Nørskov, K. Chan and H. Wang, *Nat. Catal.*, 2018, **1**, 111–119.

8 C. M. Gabardo, A. Seifitokaldani, J. P. Edwards, C.-T. Dinh, T. Burdyny, M. G. Kibria, C. P. O'Brien, E. H. Sargent and D. Sinton, *Energy Environ. Sci.*, 2018, **11**, 2531–2539.

9 D. Chen, F. Wang, Y. Liu, W. Lyu, X. Zhao, R. Fang, L. Chen and Y. Li, *Angew. Chem., Int. Ed.*, 2025, **64**, 21149–21160.

10 C. Wu, K. Song, X. Zhang, B. Tan, R. Liao, Z. Liu, H. Zhu and J. Wang, *Angew. Chem., Int. Ed.*, 2025, **64**, 23200–23210.

11 D. D. Zhu, J. L. Liu and S. Z. Qiao, *Adv. Mater.*, 2016, **28**, 3423–3452.

12 G. Wang, J. Chen, Y. Ding, P. Cai, L. Yi, Y. Li, C. Tu, Y. Hou, Z. Wen and L. Dai, *Chem. Soc. Rev.*, 2021, **50**, 4993–5061.

13 X. Wu, Y. Guo, Z. Sun, F. Xie, D. Guan, J. Dai, F. Yu, Z. Hu, Y.-C. Huang, C.-W. Pao, J.-L. Chen, W. Zhou and Z. Shao, *Nat. Commun.*, 2021, **12**, 660.

14 M. Yang, J. Wu, Y. Li, H. Pan, H. Cui, X. Lu and X. Tang, *ACS Catal.*, 2024, **14**, 6169–6178.

15 A. Sacco, R. Speranza, U. Savino, J. Zeng, M. A. Farkhondehfal, A. Lamberti, A. Chiodoni and C. F. Pirri, *ACS Sustainable Chem. Eng.*, 2020, **8**, 7563–7568.

16 C. Wang, H. Ren, Z. Wang, Q. Guan, Y. Liu and W. Li, *Appl. Catal., B*, 2022, **304**, 120958.

17 D. Wakerley, S. Lamaison, J. Wicks, A. Clemens, J. Feaster, D. Corral, S. A. Jaffer, A. Sarkar, M. Fontecave, E. B. Duoss, S. Baker, E. H. Sargent, T. F. Jaramillo and C. Hahn, *Nat. Energy*, 2022, **7**, 130–143.

18 G. Wen, B. Ren, X. Wang, D. Luo, H. Dou, Y. Zheng, R. Gao, J. Gostick, A. Yu and Z. Chen, *Nat. Energy*, 2022, **7**, 978–988.

19 M. Ma, B. J. Trześniewski, J. Xie and W. A. Smith, *Angew. Chem., Int. Ed.*, 2016, **55**, 9748–9752.

20 A. D. Handoko, F. Wei, J. Jenndy, B. S. Yeo and Z. W. Seh, *Nat. Catal.*, 2018, **1**, 922–934.

21 H. S. Jeon, I. Sinev, F. Scholten, N. J. Divins, I. Zegkinoglou, L. Pielsticker and B. R. Cuenya, *J. Am. Chem. Soc.*, 2018, **140**, 9383–9386.

22 H. Huang, Y. Zhang, W. Chen, J. Chen, X. Zou, J.-J. Lv, X. Chen, Z. Shen, Z. Ge, L. Guo, Y. Yao and Y. Wang, *Adv. Energy Mater.*, 2024, **15**, 2405534.

23 B. Ravel and M. Newville, *J. Synchrotron Radiat.*, 2005, **12**, 537–541.

24 F. D. Vila, J. J. Rehr, H. H. Rossner and H. J. Krappe, *Phys. Rev. B: Condens. Matter Mater. Phys.*, 2007, **76**, 014301.

25 A. B. Moss, S. Garg, M. Mirolo, C. A. Giron Rodriguez, R. Ilvonen, I. Chorkendorff, J. Drnec and B. Seger, *Joule*, 2023, **7**, 350–365.

26 S. Hao, A. Elgazzar, N. Ravi, T. Wi, P. Zhu, Y. Feng, Y. Xia, F. Chen, X. Shan and H. Wang, *Nat. Energy*, 2025, **10**, 266–277.

27 Z. Liu, H. Yang, R. Kutz and R. I. Masel, *J. Electrochem. Soc.*, 2018, **165**, J3371.

28 Z. Yin, H. Peng, X. Wei, H. Zhou, J. Gong, M. Huai, L. Xiao, G. Wang, J. Lu and L. Zhuang, *Energy Environ. Sci.*, 2019, **12**, 2455.

29 M. A. Blommaert, J. A. H. Verdonk, H. C. B. Blommaert, W. A. Smith and D. A. Vermaas, *ACS Appl. Mater. Interfaces*, 2020, **3**, 5804–5812.

30 A. Angulo, P. van der Linde, H. Gardeniers, M. Modestino and D. Fernández Rivas, *Joule*, 2020, **4**, 555–579.

31 S. Hao, A. Elgazzar, N. Ravi, T.-U. Wi, P. Zhu, Y. Feng, Y. Xia, F.-Y. Chen, X. Shan and H. Wang, *Nat. Energy*, 2025, **10**, 266–277.

32 L. Yuan, X. Li, G. Li, K. Peng, H. Zhang, S. Zeng, X. Sun and X. Zhang, *Adv. Sci.*, 2025, **12**, 368–378.

33 S. Yoo, S. Yoo, G. Deng, F. Sun, K. Lee, H. Jang, C. W. Lee, X. Liu, J. Jang, Q. Tang, Y. J. Hwang, T. Hyeon and M. S. Bootharaju, *Adv. Mater.*, 2023, **36**, 13032–13043.

34 Z.-Y. Wu, P. Zhu, D. A. Cullen, Y. Hu, Q.-Q. Yan, S.-C. Shen, F.-Y. Chen, H. Yu, M. Shakouri, J. D. Arregui-Mena, A. Ziabari, A. R. Paterson, H.-W. Liang and H. Wang, *Nat. Synth.*, 2022, **1**, 658–667.

35 Z. Ma, B. Wang, X. Yang, C. Ma, W. Wang, C. Chen, F. Liang, N. Zhang, H. Zhang, Y. Chu, Z. Zhuang, H. Xu, Y. Wang and J. Liu, *J. Am. Chem. Soc.*, 2024, **146**, 29140–29149.

36 K. Jiang, P. Yan, P. Shi, J. Zhang, X. Chai, Y. Wang, C. Zhu, C. Yang, C. Lu, Y. Liu, K. Cao and X. Zhuang, *Angew. Chem., Int. Ed.*, 2024, **64**, 202417658.

37 R. Kortlever, J. Shen, K. J. P. Schouten, F. Calle-Vallejo and M. T. M. Koper, *J. Phy. Chem. Lett.*, 2015, **6**, 4073–4082.

38 C. Long, X. Liu, K. Wan, Y. Jiang, P. An, C. Yang, G. Wu, W. Wang, J. Guo, L. Li, K. Pang, Q. Li, C. Cui, S. Liu, T. Tan and Z. Tang, *Sci. Adv.*, 2023, **9**, adi6119.

39 S. Liu, H. Tao, L. Zeng, Q. Liu, Z. Xu, Q. Liu and J.-L. Luo, *J. Am. Chem. Soc.*, 2017, **139**, 2160–2163.

40 X. Chen, Y. Tan, J. Yuan, S. Zhai, L. Su, Y. Mou, W. Deng and H. Wu, *Adv. Energy Mater.*, 2025, **15**, 2500872.

41 L. Yuan, S. Zeng, X. Zhang, X. Ji and S. Zhang, *Mater. Rep.: Energy*, 2023, **3**, 100177.